Synthesis of graphene by cobalt-catalyzed decomposition of methane in plasma-enhanced CVD: Optimization of experimental parameters with Taguchi method

H.-A. Mehedi, B. Baudrillart, D. Alloyeau, O. Mouhoub, C. Ricolleau, V D Pham, C. Chacon, A. Gicquel, J. Lagoute, S. Farhat

AIP Journal of Applied Physics

Synthesis of graphene by cobalt-catalyzed decomposition of methane in plasma-enhanced CVD: Optimization of experimental parameters with Taguchi method

H.-A. Mehedi, B. Baudrillart, D. Alloyeau, O. Mouhoub, C. Ricolleau, V. D. Pham, C. Chacon, A. Gicquel, J. Lagoute, and S. Farhat

Citation: Journal of Applied Physics **120**, 065304 (2016); doi: 10.1063/1.4960692
View online: http://dx.doi.org/10.1063/1.4960692
View Table of Contents: http://scitation.aip.org/content/aip/journal/jap/120/6?ver=pdfcov
Published by the AIP Publishing

Synthesis of graphene by cobalt-catalyzed decomposition of methane in plasma-enhanced CVD: Optimization of experimental parameters with Taguchi method

H.-A. Mehedi,[1] B. Baudrillart,[1] D. Alloyeau,[2] O. Mouhoub,[2] C. Ricolleau,[2] V. D. Pham,[2] C. Chacon,[2] A. Gicquel,[1] J. Lagoute,[2] and S. Farhat[1,a)]

[1]*Laboratoire des Sciences des Procédés et des Matériaux, CNRS, LSPM – UPR 3407, Université Paris 13, PRES Sorbonne-Paris-Cité, Villetaneuse 93430, France*

[2]*Laboratoire Matériaux et Phénomènes Quantiques, CNRS, UMR 7162, Université Paris Diderot, Bâtiment Condorcet, Paris 75205, France*

(Received 18 May 2016; accepted 28 July 2016; published online 11 August 2016)

This article describes the significant roles of process parameters in the deposition of graphene films via cobalt-catalyzed decomposition of methane diluted in hydrogen using plasma-enhanced chemical vapor deposition (PECVD). The influence of growth temperature (700–850 °C), molar concentration of methane (2%–20%), growth time (30–90 s), and microwave power (300–400 W) on graphene thickness and defect density is investigated using Taguchi method which enables reaching the optimal parameter settings by performing reduced number of experiments. Growth temperature is found to be the most influential parameter in minimizing the number of graphene layers, whereas microwave power has the second largest effect on crystalline quality and minor role on thickness of graphene films. The structural properties of PECVD graphene obtained with optimized synthesis conditions are investigated with Raman spectroscopy and corroborated with atomic-scale characterization performed by high-resolution transmission electron microscopy and scanning tunneling microscopy, which reveals formation of continuous film consisting of 2–7 high quality graphene layers. *Published by AIP Publishing.* [http://dx.doi.org/10.1063/1.4960692]

I. INTRODUCTION

Because of the unique properties of graphene and its potential for use in a variety of applications,[1–4] progress has been made in developing processes able to grow large-area and defect-free materials. For this purpose, several synthetic methods have exhibited some success in producing thin graphene films, including (i) the sublimation of SiC at high temperatures,[5,6] (ii) the intercalation of graphite,[7] (iii) chemically functionalized graphene reduction,[8,9] and (iv) chemical vapor deposition (CVD).[10,11]

Unsurprisingly, CVD has emerged as the most versatile and commercially viable technique for graphene production because of its successful production of various high-quality, high-performance nanomaterials.[12] Using CVD, graphene is grown onto transition metals, which enables a low-energy pathway by forming intermediate compounds for the growth of graphene.[13]

Graphene growth has been demonstrated on a number of metals, i.e., gold (Au),[14] copper (Cu),[11] cobalt (Co),[15] iridium (Ir),[16] nickel (Ni),[17,18] palladium (Pd),[19] platinum (Pt),[20] and ruthenium (Ru).[10] The first row of transition metals Co, Ni, and Cu is of great interest due to their low cost and high availability. The difference in the carbon solubility between these metals leads to different growth procedures and also impacts the growth quality. Unlike Cu which has the lowest carbon solubility, cobalt can dissolve large amounts of carbon in their bulk, and hence, the growth mechanism is mainly precipitation based, with additional contributions from precursor decomposition on the metal surface.[21] During cooling, the carbon from the bulk precipitates in the lowest free energy state (graphene) on the surface.

The type of activation energy that must be supplied to sustain chemical reactions is critical because it affects the rate of production of the active carbon species (CH_3, CH_2, CH, C_2, C, etc.) that subsequently react to produce graphene. Accordingly, a key parameter to take into account is the dehydrogenation energy of the precursor (CH_x to CH_{x-1}). Methane, the most used carbon precursor, is a highly stable, saturated molecule, so the dehydrogenation in the gas phase of CH_x to CH_{x-1} is highly endothermic (440 kJ mol^{-1}) and its thermal (non-catalytic or non-plasma-activated) decomposition occurs at relatively high temperatures (>1200 °C).[22] However, on the metal surface, there is a significant reduction of the energy required, owing to the presence of strong metal–CH_{x-1} and metal-H interactions.[22] This catalytic behavior is observed when growing CVD-produced graphene on metals at low temperatures (<900 °C) to a greater or lesser extent.[23] Therefore, non-catalytic activation can be considered negligible when working in thermal systems. In thermal CVD, the heat energy is supplied through horizontal or vertical tubes with hot walls (mostly used in graphene synthesis), i.e., the reactor walls are heated by a surrounding furnace or by external radiofrequency or infrared radiation. The reactor operates through the batch processing of wafers with good radial uniformity but more suspect axial uniformity. The process is not transport limited and has a slow growth rate and high temperature dependence. To avoid

a)Author to whom correspondence should be addressed. Electronic mail: samir.farhat@lspm.cnrs.fr.

these problems, plasma-enhanced CVD, a variant of thermal CVD, was proposed as an alternative approach for graphene synthesis. Plasma-enhanced processing uses, in general, showerhead reactors with single-wafer and cold-wall designs because only the substrate is heated by resistive heating and/or plasma heating in the vicinity of the substrate. Thus, the reaction rate is reduced, but the film quality can be better controlled. The plasma and metal coupling cause localized rapid heating of the metal catalyst, which reduces the heating time. The plasma can provide a rich chemical environment, including a mixture of radicals, molecules, and ions, from a simple hydrogen-hydrocarbon feedstock.[24] The ions impart their energy and momentum to the reactant gas molecules and atoms. The energy transfer breaks up the molecules and benefits the chemical reactions, allowing for lower deposition temperatures and faster growth than thermal CVD. Recent years have witnessed advances in plasma-enhanced chemical vapor deposition (PECVD) synthesis of graphene,[25–31] and over substrates other than those used in standard processes such as glass,[31] enabling the full exploitation of graphene properties and application potentials. Therefore, plasma-assisted deposition could be a potential process in the future development of graphene.

To date, the quality of PECVD-grown graphene has not been significantly better than that of thermal CVD.[25–31] The high defect density commonly observed in PECVD graphene is referred to energetic particles from the plasma interacting with the growing surface. For graphene materials to realize the promise of "graphene-based applications," it is clearly necessary to solve those problems, preventing defects in fabricated large area devices. Since the large-scale graphene films synthesized on Ni or Co so far have typically been polycrystalline (mixture of monolayer and few layers graphene), the research effort is aimed to control the domain size, the number of graphene layers, and the defect density.

In PECVD process, electron gas-phase reactions must be taken into account and graphene growth cannot then be considered as totally controlled by the catalyst. Additional process parameters such as plasma power must be considered to control species distribution. In addition, depending on the horizontal or vertical reactor position, gas-phase temperature gradients can produce density variations leading to buoyancy-driven secondary flows superimposed on the main flow of the active carbon species which adversely affect gas-phase reactions and species' spatial distributions. Depending on the configuration of the plasma reactor and the type of catalyst used, many process parameters may affect graphene quality. As a result, it becomes time consuming to find out the optimum conditions in such high dimensional parameter space. In such situation, Taguchi technique provides an efficient and systematic method to optimize the system. It is an empirical approach that combines mathematical and statistical techniques and utilizes orthogonal arrays (OAs) to study a large number of variables using a small number of trials.[32,33] Another important point is that many different variables can be examined simultaneously. This means that predominant parameters can be investigated deeply, whereas secondary parameters can be overlooked. Therefore, time, energy, and resources can be saved. The Taguchi method was employed in optimizing the production of materials in different forms, such as diamond-like carbons,[34] polycrystalline diamond coatings,[35] carbon nanotubes,[36] and graphene films by copper-catalyzed decomposition of ethanol.[37]

Here, we utilize Taguchi method to optimize the synthesis of graphene with PECVD and to find the most suitable experimental conditions for the production of highly crystalline thin films by cobalt catalyzed decomposition of methane (CH_4). The optimization procedure proceeds through: (1) selection of the parameters (control factors) governing the PECVD process of graphene and choice of their levels; (2) design and running of experiments to investigate the parameters' influence on the process; and (3) running of new experiments to test the configurations under which the process is predicted to give optimal responses.[37]

Four experimental parameters, such as growth temperature (700–850 °C), CH_4 concentration (2%–20%), growth time (30–90 s), and microwave power (300–400 W), are investigated and optimized using a 2-level Taguchi design[32,33] to minimize the number of graphene layers and the density of lattice defects. To monitor the results of the Taguchi experiments, the graphene films are systematically investigated by Raman spectroscopy. Then, analysis of variance (ANOVA) and signal-to-noise (SN) analysis available in Qualitek-4 (QT4) software were used to monitor the parameter influence and optimize the process. Graphene films grown under the optimized conditions are further characterized by high-resolution transmission electron microscopy (HRTEM) and scanning tunneling microscopy (STM). For this purpose, as-grown graphene films are transferred from Co substrates to the TEM grid and mica/gold substrate (for STM) using a non-destructive and rapid-transfer bubbling technique which is based on the mechanical separation of graphene from the substrate by H_2 bubbles during H_2O electrolysis requiring only a few tens of seconds and leaves the Co substrate intact.[23]

II. EXPERIMENTAL

A. Taguchi design of PECVD experiments

A set of PECVD experiments was designed to investigate the most influential parameters in the cobalt-catalyzed synthesis of graphene films. The following four parameters were assumed to exert the most control over the process as indicated by the graphene thickness and defect density: (1) substrate temperature (T_s), (2) methane flow rate (Φ_{CH4}), (3) growth time (t), and (4) microwave power (P_{mw}). Each control factor was varied at the following two levels: $T_s = 700$ °C or 850 °C, $\Phi_{CH4} = 1$ sccm or 10 sccm, $t = 30$ s or 90 s, and $P_{mw} = 300$ W or 400 W; the effects of these variations were investigated. The corresponding design of experiments (DOE) is reported in Table I. The samples obtained under the DOE experimental settings are labeled as DN with N being between 1 and 8.

The selection of the control factors and their levels was imposed by the design of our reactor. Because microwave plasma contributes to the heating of the substrate, the combination of gas pressure and substrate position relative to the center of the plasma must be fixed to control the temperature

TABLE I. Taguchi-designed trial experiments for graphene PECVD.

	Control factors			
Experiments[a]	T_s (°C)	Φ_{CH4} (sccm)	t (s)	P_{mw} (W)
D1	700	1	30	300
D2	700	1	90	400
D3	700	10	30	400
D4	700	10	90	300
D5	850	1	30	400
D6	850	1	90	300
D7	850	10	30	300
D8	850	10	90	400

[a]50 sccm H_2 is used as a carrier gas; 100 sccm Ar for cooling; chamber pressure is maintained at 8 mbar for 300 W and 13 mbar for 400 W in order to maintain a constant plasma volume.

as P_{mw} is varied. This parameter was varied between 300 and 400 W to ensure a balance between its thermal contribution and the damage induced during graphene growth. We fixed the annealing time at 10 min and the hydrogen flow rate at 50 sccm (for both the annealing and growth steps), and the cooling conditions were kept constant by fixing argon flow rate to 100 sccm.

It has been generally accepted that cobalt, nickel, and iron show the highest catalytic activity for the growth of carbon nanomaterials, including carbon nanotubes (CNTs) and graphene.[38] However, because of their high carbon solubility, uncontrollable precipitation in cooling process may affect the quality and uniformity of the graphene. Two major factors can affect graphene formation in such situation: (i) cooling rate and (ii) carbon concentration at the cobalt surface. Since we used commercial cobalt foil, this made difficult to precisely control the precipitation process by adding a supplementary parameter in Taguchi optimisation procedure. The reason is the complex bulk diffusion in polycrystalline substrates. Hence, we fixed the cooling rate at its maximum value and developed a strategy to optimize the carbon concentration on the top of the cobalt surface by adjusting process parameters as pressure, microwave power, carbon concentration, and substrate temperature which, so far, is more reproducible control. A basic understanding of the complex gaseous and surface processes involved in graphene CVD is schematically shown in Figure S1 in the supplementary material.

B. Graphene deposition

We conducted graphene PECVD using a 10-cm-diameter vertical silica bell jar low-pressure reactor (Figure 1(a)) with CH_4 as the carbon precursor and 125–μm-thick polycrystalline cobalt foil (99.9% purity, *GoodFellow Gmbh*) as the substrate. For plasma generation, the reactor utilized a 1.2 kW microwave generator (SAIREM) operating at 2.45 GHz. The electromagnetic waves were generated, guided using a rectangular wave guide, and directed into a cavity delimited by a Faraday cage. The short-circuit piston at the end of the wave guide helped create stationary waves and situate the maximum of the electric field near the substrate. Efficient operation was assumed with good microwave coupling and minimal radial diffusion to the quartz enclosure, leading to greater discharge stability and better plasma uniformity. Input power was varied with the pressure simultaneously in order to hold plasma volume constant. As shown in Figure 1(a), a quasi-hemispherical

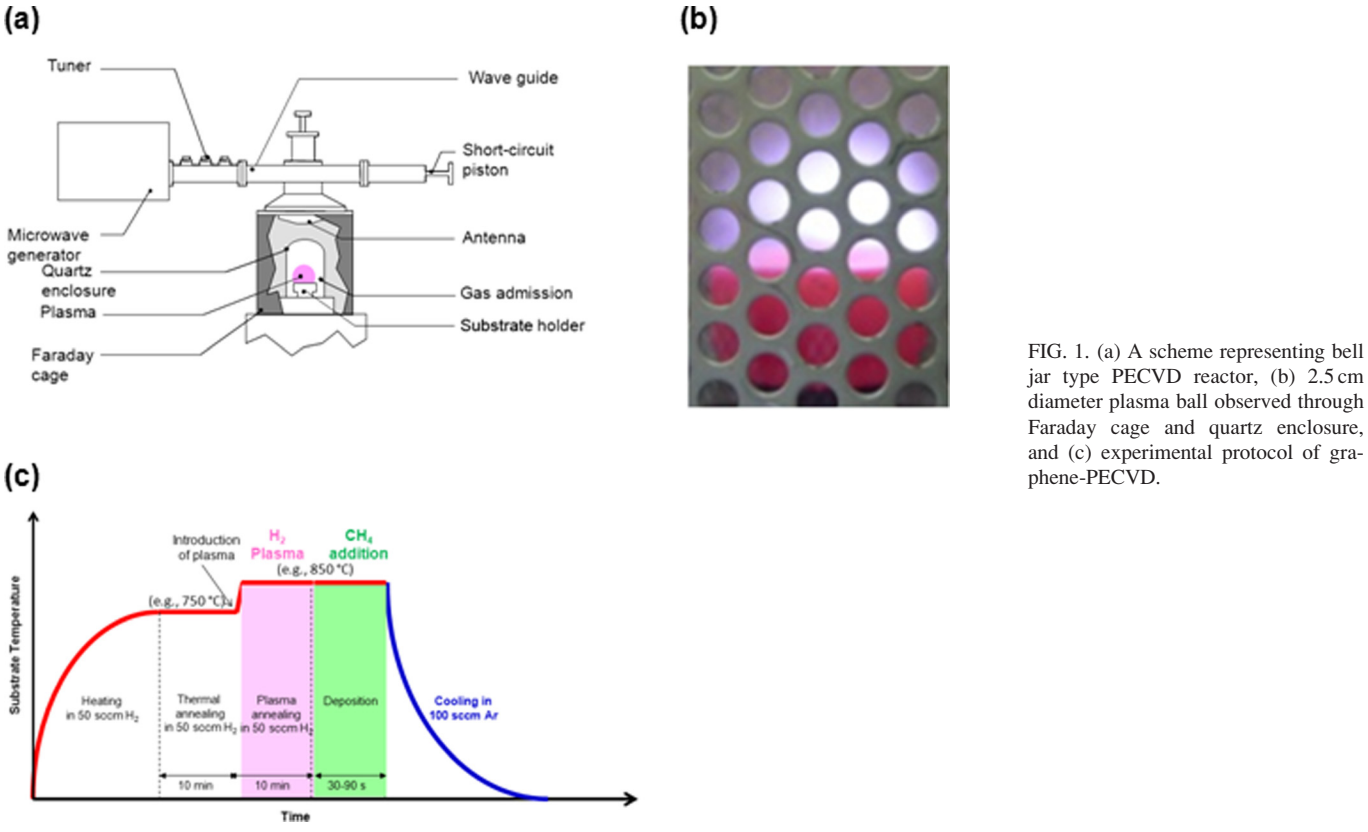

FIG. 1. (a) A scheme representing bell jar type PECVD reactor, (b) 2.5 cm diameter plasma ball observed through Faraday cage and quartz enclosure, and (c) experimental protocol of graphene-PECVD.

active plasma zone of radius of ~2.5 cm was created near the substrate. The input gases ($CH_4/H_2/Ar$) with electronically controlled mass flow rates were injected into the reactor and pumped out by the reactor pumping system. The cobalt substrate (~$3 \times 3\,cm^2$ in size) was placed on a resistive molybdenum boat (substrate holder). Substrate heating was achieved by flowing electric current from an external heating unit through a graphite resistor placed below the molybdenum holder. The heating unit was designed to automatically adjust the current flow with respect to the temperature measured by the thermocouple embedded in the substrate holder. During all the experiments, the substrate temperature was monitored by an optical pyrometer (IMPAC, IGAQ-10), and we considered this temperature to be the actual substrate/deposition temperature for graphene synthesis.

Prior to growth, the substrates were first cleaned with acetone and then isopropanol in an ultrasonic bath to remove residual oxides. After loading the substrate, the reactor was pumped down to the base pressure, which was as low as 10^{-7} mbar. The synthesis process, as detailed in Figure 1(c), began with substrate heating in a hydrogen atmosphere with a 50-sccm flow rate. Once the desired annealing temperature was achieved, a 10-min annealing step was conducted, allowing temperature stabilization, residual oxide removal, and cobalt grain growth. Then, the annealing was continued for another 10 min in the presence of plasma to further remove any trace of oxides. Note that the temperature increased at the onset of the plasma, indicating the thermal contribution of the plasma. At the end of this period, growth was initiated by introducing methane.

The end of the growth phase was signaled by stopping the plasma, heating and gas flow, and immediately injecting 100-sccm Ar flow into the reactor, thereby cooling it to room temperature (cooling stage). The temperature decreased abruptly (approximately 200 °C within a second) immediately after the plasma was turned off and then cooling proceeded at ~100 °C/min to 400 °C, followed by 20 °C/min to room temperature.

C. Transfer of graphene via bubbling transfer method

We used the electrolysis bubbling-assisted transfer approach[23] to transfer graphene from the Co-substrates to a TEM grid and a gold/mica substrate for HRTEM and STM characterization, respectively. In this process, a polymer (poly-methylmethacrylate, PMMA) layer was first spin-coated on graphene/cobalt samples (5000 rpm, 1 min post-baking at 180 °C). The PMMA layer acts as a supporting scaffold, preventing the graphene film from rolling or tearing during the peeling process. The PMMA/graphene/cobalt bundle was then used as the cathode of an electrolytic cell. A cobalt foil was used for the anode, and an aqueous solution of NaOH (1 M) was employed as the electrolyte. During the electrochemical etching, direct current (dc) voltage was applied to the electrodes, and hydrogen bubbles were created at the graphene/cobalt interfaces because of the reduction of water in the electrolytic cell

$$2H_2O\,(l) + 2e^- \rightarrow H_2(g) + 2OH^-(aq).$$

These H_2 bubbles provide a gentle but persistent force to detach the graphene film from the cobalt substrate at its edges.[23]

The typical time required for the complete delamination of the PMMA/graphene bundle from the cobalt substrate was ~30 s. Subsequently, the PMMA/graphene bundle was lifted and rinsed in a deionized water bath to remove residual electrolyte. It was then placed on the target substrate (PMMA/graphene/target substrate, in this order). Because of the delicate nature of the target substrate, this bundle was dried at room temperature or on a hot plate at 50 °C. PMMA was then removed by immersing the sample in an acetone bath.

D. Characterization

Characterization of the as-grown films on the cobalt substrates began with room temperature Raman spectroscopy (*HR800*, HORIBA Jobin-Yvon) in confocal mode in air with the back-scattering configuration using 632.8-nm laser excitation to identify the crystalline quality and graphene thickness. Three different locations were probed to describe each specimen reliably and discard possible spatial inhomogeneities. An acquisition time of 45 s was used to obtain a sufficient signal-to-noise ratio. The spectra were averaged, normalized, and analyzed using a commercially available spectroscopic analysis software package. The morphology of the deposited films with optimum PECVD conditions was evaluated by means of HRTEM and STM after transferring the as-grown films onto TEM-grids and Au (111)/mica substrates, respectively.

Quantitative HRTEM analyses of PECVD graphene were performed by using a JEM-ARM200F microscope. The combination of the JEOL cold FEG and the CEOS corrector to compensate the spherical aberration of the objective lens allows acquiring images at 80 kV with sub-angstrom resolution and high sensitivity.[39] In order to identify single layer area, HRTEM images were simulated with the JEMS software, by using the aberration coefficients experimentally calculated by the CEOS corrector software (spherical aberration coefficient and the defocus spread were 0.006 mm and 5.5 nm, respectively).[40]

III. RESULTS AND DISCUSSION

A. Results of Taguchi-designed experiments

The Raman spectrum of graphene collected with 632.8-nm laser excitation is composed of three major peaks: (1) The D-band, centered at ~$1328\,cm^{-1}$, is attributed to disorder-induced first-order scattering (interlayer effects); (2) the G-band at ~$1583\,cm^{-1}$ is a result of in-plane (intralayer) vibrations of the sp^2-hybridized carbon atoms; and (3) the 2D-band located at approximately $2700\,cm^{-1}$ is an overtone of the D-band and can be attributed to a two-phonon double resonance Raman process.[41–44] Based on these characteristic peak positions, shapes, and relative intensities, information about the number of layers (I_{2D}/I_G) and the density of the lattice defects (I_D/I_G) in a graphene sample can be determined. Single-layer graphene, particularly that produced by mechanical exfoliation, is characterized by a very

sharp symmetrical Lorentzian 2D peak (full width at half maximum [FWHM] $\sim 24\,cm^{-1}$), and its intensity is more than twice that of the G peak ($I_{2D}/I_G > 2$).[42,44] In CVD graphene, the shape difference of the 2D peak for one or more layers is not as clear as that of exfoliated graphene because of the lower electronic coupling between layers with unordered stacking. In addition, as the number of layers increases, the 2D peak becomes broader and less symmetrical, and its intensity decreases.[42] In multilayer graphene, interlayer interactions and twist angle can also affect peak position and intensity.[45]

Figure 2 shows the Raman spectra of the as-deposited films on cobalt substrates obtained using the experimental configurations summarized in Table I. The spectra show three main features, as mentioned above, in the 1200–2900 region, D-band ($\sim 1330\,cm^{-1}$), the G-band ($\sim 1382\,cm^{-1}$), and the 2D-band ($\sim 2680\,cm^{-1}$). The extracted 2D/G and D/G intensity ratios are listed in Table II. Each value was determined using the average results obtained by measuring Raman scattering at three different locations on the sample. The variation of the selected control factors caused I_D/I_G and I_{2D}/I_G to vary around mean values of 0.77 and 0.38, respectively, revealing that the deposited films generally consist of multiple defective graphene layers. Defects could be associated with graphene edges or Stone-Wales pentagon-heptagon defects in graphene lattice.[42]

B. Influences of experimental parameters

The Taguchi method allows us to quantify the influence of the selected experimental parameters (T_s, t, Φ_{CH4}, and P_{mw}) on graphene thickness and defect density. To do so, the S/N ratio of the collected outputs (I_{2D}/I_G and I_D/I_G) was analyzed. The S/N ratio for the I_{2D}/I_G output response (which should be maximized to grow graphene films with fewer layers) was calculated as

$$\left(\frac{S}{N}\right)_{larger-is-better} = -10\,\log_{10}\left[\frac{1}{n}\sum_{i=1}^{n}\left(\frac{1}{Y_i^2}\right)\right], \qquad (1)$$

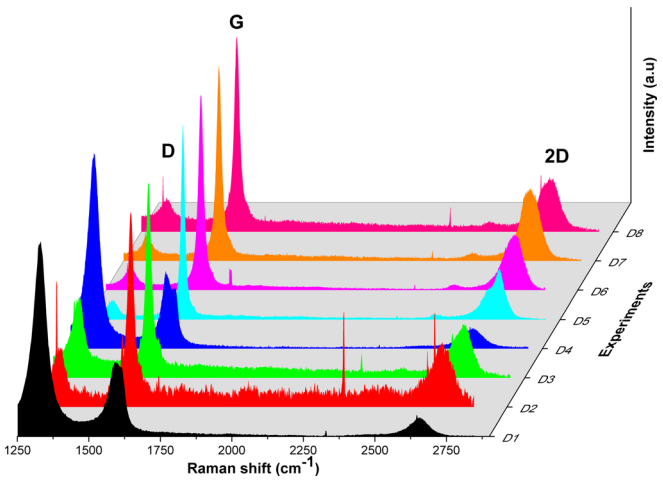

FIG. 2. Raman spectra of the graphene films at 632 nm laser excitation obtained in trial experiments (D1 to D8). Spectra are normalized to the corresponding band maximum intensity.

TABLE II. Results of Taguchi-designed CVD growth experiments in terms of structural properties of the synthesized samples, as described by Raman indicators I_D/I_G and I_{2D}/I_G, respectively, monitoring density of lattice defects and number of layers. The corresponding S/N ratios and average values are also reported.

	I_D/I_G		I_{2D}/I_G	
Experiments	Data	S/N (dB)	Data	S/N (dB)
D1	1.85	−5.53	0.50	−6.67
D2	0.49	6.19	0.51	−7.54
D3	0.43	7.21	0.36	−8.97
D4	2.36	−7.45	0.31	−10.42
D5	0.31	9.56	0.34	−10.05
D6	0.15	15.22	0.32	−9.84
D7	0.26	11.55	0.37	−9.22
D8	0.28	10.97	0.37	−8.75
Average values	0.77	5.96	0.38	−8.93

whereas for the I_D/I_G output response, the S/N ratio (which should be minimized to reduce the defect density in the graphitic lattice) was

$$\left(\frac{S}{N}\right)_{smaller-is-better} = -10\,\log_{10}\left[\frac{1}{n}\sum_{i=1}^{n}(Y_i^2)\right]. \qquad (2)$$

In both cases, n is the number of measurements in each experiment, and Y_i is the investigated outputs (I_{2D}/I_G and I_D/I_G) for ith experiment. The S/N ratios obtained by analyzing raw I_{2D}/I_G and I_D/I_G data are reported in Table II. Based on these values, the mean S/N ratios for each selected parameter were calculated by averaging on each level. For instance, synthesis temperature (T_s) was varied in two levels (700 and 850 °C) which resulted in four Taguchi trial experiments for each temperature (Table I); the mean S/N ratio for 700 °C was determined by averaging the S/N ratios obtained in the Taguchi experiments of D1 to D4. The mean S/N ratios are plotted in Figure 3.

According to Equations (1) and (2), optimizing the physical quantities Y requires maximizing the corresponding S/N ratio because larger S/N ratios correspond to lower response variability.[32–37] Therefore, the control factor producing the greatest S/N variation is the most influential on the considered output.[32–37] For instance, in the case of the larger-is-better analysis of graphene thickness (Figure 3(a)), the greatest variation of the S/N ratio was observed for the substrate temperature, T_s (1.06 dB) revealing that this parameter has the greatest influence on graphene thickness, whereas microwave power P_{mw}, which resulted in the smallest (0.21 dB) S/N variation, is the least influential factor. Similarly, in the case of the smaller-is-better analysis of defect density (Figure 3(b)), temperature had the most important influence on defectiveness in graphene, and microwave power has the second largest effect. Both the larger-is-better and smaller-is-better analyses suggest that substrate temperature has the greatest influence on the overall quality of graphene. Figures 3(c) and 3(d) show the degree of influence of each factor on I_{2D}/I_G and I_D/I_G, respectively, which was calculated using the following equation:

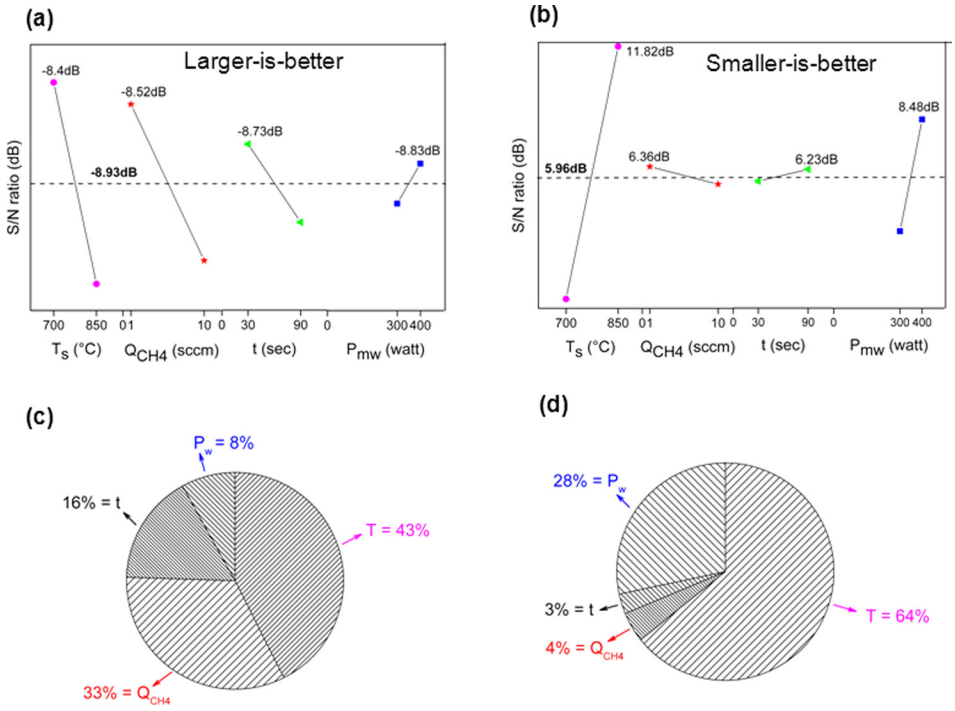

FIG. 3. Response graphs of S/N ratio for (a) "larger-is-better" analysis of I_{2D}/I_G and for (b) "smaller-is-better" analysis of I_D/I_G. In each response graph, dashed line indicates the total mean S/N ratio; for each control-factor, the greatest S/N value is also reported. The degree of influence of the control factors on I_{2D}/I_G (c) and I_D/I_G (d) is displayed.

$$I_k = 100\left(\frac{\Delta R_k}{\Delta R_{tot}}\right), \tag{3}$$

where $\Delta R_k = \left(\frac{S}{N}\right)_k^{max} - \left(\frac{S}{N}\right)_k^{min}$ is the variation associated with the changes of the kth factor and $\Delta R_{tot} = \sum_{k=1}^{F} \Delta R_k$ is the sum of the variations associated with the changes of all the factors F.

C. Optimal conditions and results

Because the highest S/N ratio indicates the optimal level of each control factor, from the results of the "larger-is-better" analysis of S/N shown in Figure 3(a), we expect that within the ranges of the T_s, Φ_{CH4}, t, and P_{mw} considered, the optimal yield of few-layer graphene films via PECVD occurs at $T_s = 700\,^{\circ}C$, $\Phi_{CH4} = 1$ sccm, $t = 30$ s, and $P_{mw} = 400$ W. Additionally, the results of the "smaller-is-better" S/N analysis shown in Figure 3(b) indicate that the defect density in a graphene sample (I_D/I_G) can be minimized by selecting $T_s = 850\,^{\circ}C$, $\Phi_{CH4} = 1$ sccm, $t = 90$ min, and $P_{mw} = 400$ W. These are the two optimal configurations that are expected to yield the largest 2D/G and smallest D/G intensity ratios. Taguchi method was applied to predict the expected I_{2D}/I_D and I_D/I_G with these configurations by first calculating the predicted S/N ratio as

$$\left(\frac{S}{N}\right)_{pred} = \left(\frac{S}{N}\right)_{mean} + \sum_{k=1}^{P}\left[\left(\frac{S}{N}\right)_k^{max} - \left(\frac{S}{N}\right)_{mean}\right], \tag{4}$$

where $\left(\frac{S}{N}\right)_{mean}$ (dashed line in the response graphs of Figures 3(a) and 3(b)) is averaged across all levels of all selected parameters P, and $\left(\frac{S}{N}\right)_k^{max}$ is the largest mean S/N ratio corresponding to the optimal level of the parameter.[32,37] From $\left(\frac{S}{N}\right)_{pred}$, the predicted value of the physical quantity Y is finally estimated as

$$Y_{pred} = 10^{\frac{A}{B}} \tag{5}$$

with $A = -\frac{1}{10}\left(\frac{S}{N}\right)_{pred}$, and $B = -2$ for a larger-is-better analysis or $B = 2$ for a smaller-is-better analysis.[32,37] Inserting the values reported in Figures 3(a) and 3(b) into Eqs. (4) and (5) generates the predicted values for $(I_{2D}/I_G)_{pred} = 0.5$ and $(I_D/I_G)_{pred} = 0.2$.

To test this prediction, two additional experiments (OPT1 and OPT2 in Table III) were performed, and the Raman spectra of the corresponding films are shown in Figure 4.

The value of the 2D/G intensity ratio (0.3) obtained in OPT1 failed to meet the expectation (expected $I_{2D}/I_G = 0.5$). This shortcoming indicates that interactions occur between the parameters determining this response. In contrast, the I_D/I_G value (0.04) achieved in OPT2 was even smaller than the expected value (0.2).

Understanding the interaction between factors might provide better insight into the overall process analysis. For this purpose, the severity index, which reflects the extent of the interaction between two chosen parameters, should be estimated for each pair of control parameter.[32–37] In the present case, interaction between parameters was not considered during the design of Taguchi experiments; only the individual

TABLE III. Experimental configurations of first test-experiments and the results obtained.

	Control factors				Measured system response	
Experiments[a]	T_s	Φ_{CH4}	t	P_{mw}	I_{2D}/I_G	I_D/I_G
OPT1	700	1	30	400	0.3	0.4
OPT2	850	1	90	400	0.25	0.04

[a]50 sccm H_2 is used as a carrier gas; 100 sccm Ar for cooling; and the chamber pressure is maintained at 13 mbar.

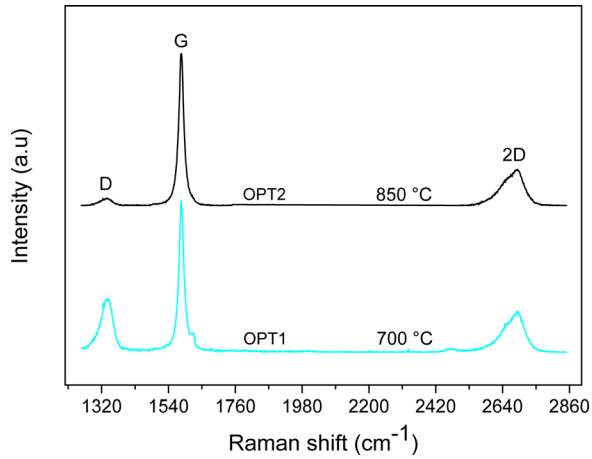

FIG. 4. Raman spectra of the as-deposited films on cobalt substrates obtained in test experiments OPT1 and OPT2 at 632 nm laser excitation. Spectra are normalized to the corresponding maximum band intensity. The spectra are shifted vertically for clarity.

influence of each chosen parameter was studied. However, if the interaction between parameters is considered, the percentage contribution of each selected parameter (T_s, Φ_{CH4}, t, and P_{mw}) to the graphene thickness (I_{2D}/I_G) and defectiveness (I_D/I_G) can be quantified by the Analysis of Variance (ANOVA) calculation with Taguchi experimental design software, Qualitek4.[32]

The mutual interaction between deposition time (t) and CH_4 flow rate (Φ_{CH4}) had the greatest influence on the graphene thickness (Figure 5(a)). The existence of this interaction might explain why the optimal configuration in OPT1 did not satisfy the expectation, despite setting all control parameters to the corresponding optimal levels needed to maximize I_{2D}/I_G. As shown in Figure 5(b), substrate temperature (Ts) has the greatest influence on defect density of the obtained graphene films, validating the reduced I_D/I_G value (0.04) obtained in OPT2 (Table III). Since simultaneous reduction of defect density and number of graphene layers requires a compromise, a new set of experiments (OPT3 and OPT4 in Table IV) was performed. Methane flow rate Φ_{CH4} was set to 1 sccm because this value should reduce the film thickness without dramatically enhancing the defect density (see the S/N changes caused by the variation of Φ_{CH4} in Figures 3(a) and 3(b)). The response graphs in Figure 3(a)

TABLE IV. Experimental configurations of second test-experiments and the results obtained.

	Control factors				Measured system response	
Experiments[a]	T_S	Φ_{CH4}	t_S	P_W	I_{2D}/I_G	I_D/I_G
OPT3	870	1	90	400	1.9	0.04
OPT4	890	1	90	400	1.2	0.04

[a]50 sccm H_2 is used as a carrier gas; 100 sccm Ar for cooling; and the chamber pressure is maintained at 13 mbar

indicate that the shorter deposition time (t = 30 s) favored the formation of thin graphene films and that the longer deposition time (t = 90 s) lowered the defect density (Figure 3(b)). Moreover, as shown in Figure 5, a significant mutual interaction exists between t and Φ_{CH4}. Therefore, optimizing the deposition time requires compromise in choosing the value of Φ_{CH4}. For a lower value of Φ_{CH4}, a longer deposition time is preferable because it positively affects defectiveness. Using higher P_{mw} (400 W) was found to benefit graphene thickness and defect density (see the S/N changes caused by varying P_{mw} in Figures 3(a) and 3(b)). The graphene films obtained under these conditions (Table IV) exhibited the same I_D/I_G value (defectiveness) as in OPT2 but had a higher 2D/G intensity ratio, confirming that temperature exerts the largest influence on graphene thickness and also validating the choice of varying the substrate temperature in the second-test experiments given in Table IV.

The measured I_{2D}/I_G ratios and the FWHM values of the 2D band of both samples were in the range of 1–2 and 35–45 cm^{-1}, respectively. These values are comparable to those of the thermal CVD-grown few-layer (2–3) graphene films.[44] Note that each of these I_{2D}/I_G ratios was calculated using the average results obtained by measuring Raman scattering at three different positions on the sample. To determine the graphene films' homogeneity over the substrate, Raman mapping was performed over an area of $100 \times 100\ \mu m^2$ (randomly selected) for sample OPT3. Figure 6(b) displays spatial inhomogeneity of the sample with around 100% surface coverage with graphene. The calculated fraction of the surface with I_{2D}/I_G higher than 1 is around 19.3%, indicating the fraction of few layer graphene in these samples. Additional SEM image of sample OPT3 is shown in Figure S2 (in the

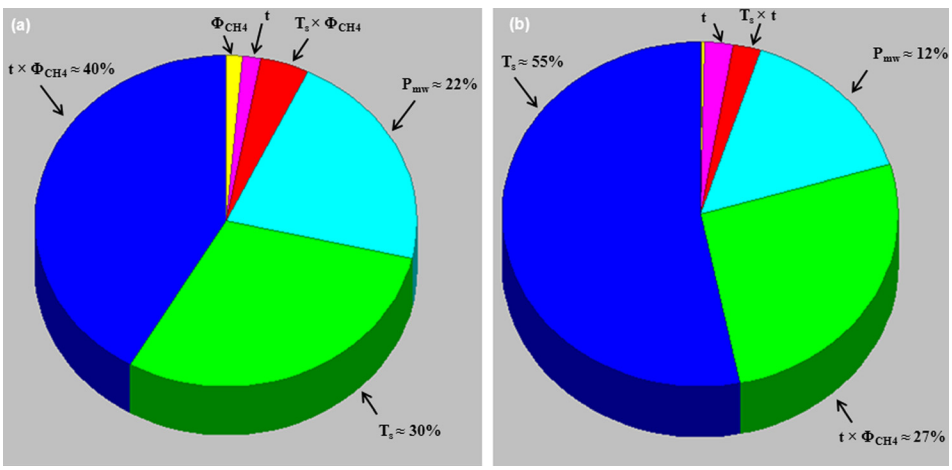

FIG. 5. Influence of growth parameters on (a) graphene thickness, I_{2D}/I_G and (b) defect density in graphitic lattice, I_D/I_G, when the interaction between parameters is considered.

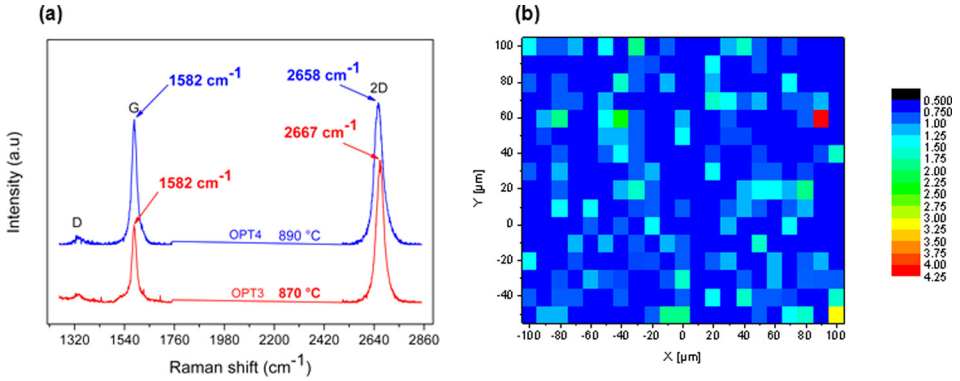

FIG. 6. (a) Raman spectra of the as-deposited graphene films on cobalt substrates obtained in test experiments OPT3 and OPT4 at 632 nm laser excitation. Spectra are normalized to the corresponding maximum band intensity. The spectra are shifted vertically for clarity. (b) Raman map of I_{2D}/I_G ratio at 632 nm laser excitation for graphene films obtained in OPT3 experiment.

supplementary material) that confirms large surface coverage of cobalt substrate with graphene films. Dark regions represent the graphene areas separated by bright ripples corresponding to cobalt grain boundaries.

After transferring the sample OPT3 on a TEM grid (see methods), we have exploited aberration-corrected HRTEM to confirm these structural information. Quantifying the number of layers in graphene by HRTEM requires to precisely tune the optical parameters of the microscope and to compare experimental images with simulations. Image aberrations were frequently determined and adjusted by using the corrector software. The focus of the images was systematically tuned to −18 nm by visualizing the size of the Thon ring that can be seen on the Fourier transform of HRTEM images when amorphous adsorbents partially cover the graphene surface. These optical conditions are precisely adjustable because the first Thon ring, corresponding to the second extremum of the contrast transfer function, then overlaps the first order reflections of the graphene structure (Figure 7(a)).[46] Besides, as illustrated on the simulated images of Bernal graphene structures with an incremental number of layers (Figure 7(b)), these optical conditions allow distinguishing single layer areas from multi-layer areas. Indeed, by comparing the simulated images with the projected atomic positions used for these simulations (left images in Fig. 7(c)), we can see that the image of a single layer is the only one which directly represents the atomic structure with bright atomic contrast and dark holes. On the contrary, the images of multilayer graphene do not show all the atomic columns of the structure, but they display a hexagonal pattern of bright dots that is similar to the image of a single layer graphene with dark atomic contrast and bright holes.

In line with the Raman measurements, HRTEM analyses revealed that PECVD samples are inhomogeneous in

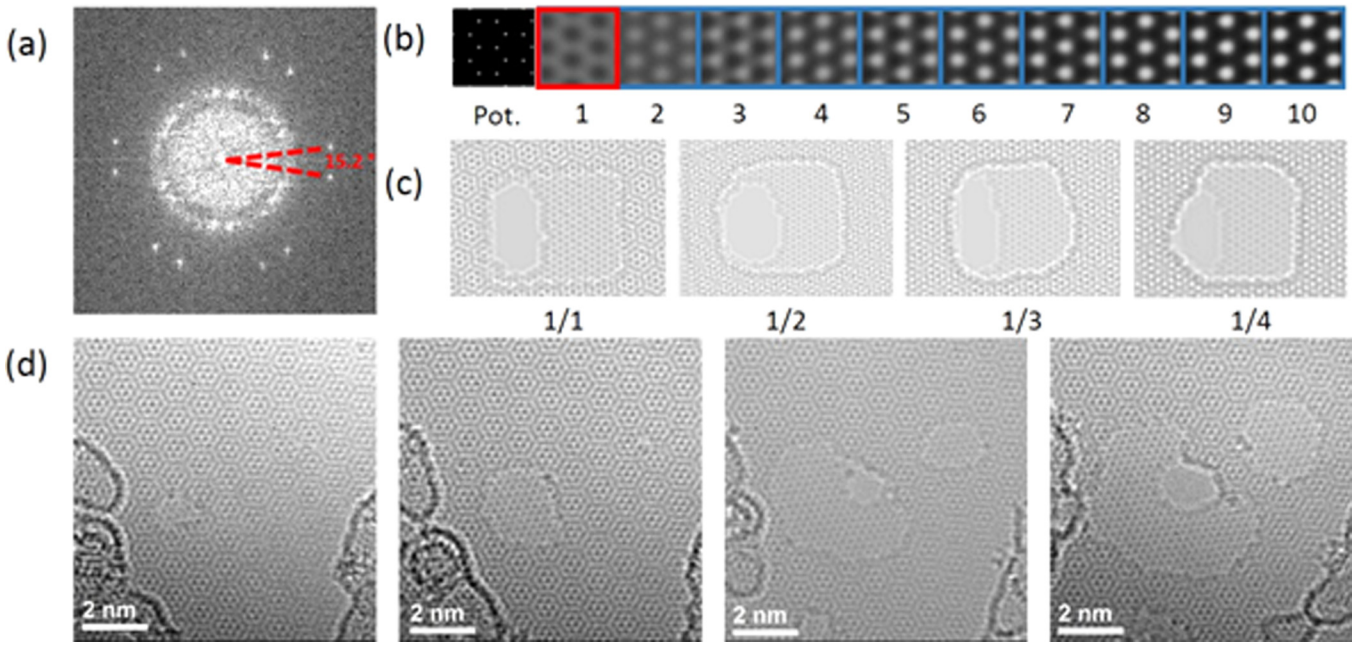

FIG. 7. HRTEM analyses of PECVD graphene. (a) Fourier transform of a HRTEM image of a twisted-multilayer graphene acquired with a focus of −18 nm. The twist angle of 15.2° between the two graphene lattices is indicated. (b) HRTEM image simulations of Bernal graphene calculated with the aberration coefficients determined experimentally (spherical aberration coefficient = 0.006 mm, defocus spread = 5.5 mm, and focus = −18 nm). The number of layers in the structure is given below each image. The two images on the left show the projected atomic positions of the single layer and multi-layer structures, respectively. (c) HRTEM image simulations of 15.2°-twisted-multilayer graphene calculated with the same optical condition than in (b). The number of layers in the lower/upper lattices is indicated below each image. The holes of different size at the center of each lattice allow observing the contrast of the lower lattice (single layer) and the Moiré pattern induced by the stacking of the two lattices. (d) HRTEM image series of a layer-by-layer peeling induced by the electron beam in a 15.2°-twisted-bilayer graphene.

structure. We identified areas with Bernal (Figure S3 in the supplementary material) and twisted multilayer graphene (Figure 7). We exploited the layer-by-layer peeling induced by the electron beam to create terraces within these multilayer graphitic structures that allow determining the number of layers. Many areas were found to have 4 to 7 layers, but several bilayer areas were also unambiguously identified. As illustrated in Figure 7(d), these bilayer areas display a well-defined Moiré pattern at the early stage of HRTEM observations. Thereafter, the electron-irradiation creates a hole in the upper layer that allows observing characteristic atomic contrast of single layer graphene. Later on, this single layer is also drilled by the electron beam and a hole with no atomic contrast appears. The structure of this twisted-bilayer area was also confirmed with image simulations of 15.2°-twisted-multilayer graphene with an incremental number of layers in the upper lattice. Indeed, the experimental Moiré pattern (Figure 7(d)) only corresponds to the simulated contrasts of a bilayer structure (Figure 7(c)).

In addition to the investigated parameters, the nature of the carbon source could influence the graphene growth, as was demonstrated by Kim *et al.*[47] They compared different carbon precursors, such as methane and acetylene, diluted in hydrogen and decomposed over nickel substrates under a variety of growth conditions. In addition, hybrid CVD machine allows testing PECVD and thermal CVD. According to this work, it is not easy to synthesize graphene at 750 °C by methane, while few layered graphene was obtained at 750 °C by acetylene.

Indeed, methane has a higher dissociation temperature than acetylene because the barrier energy for breaking the C-C bond is lower than for C-H bonds. Since carbon solubility in cobalt is similar to that in nickel, one can extrapolate the results of Kim *et al*. Nevertheless, our conditions are different from Kim *et al*. since the hydrogen to methane ratio is much larger, 50:1 H2:CH4 in our case against 15:1 H2:C2H2.[47] This leads to an excess of molecular hydrogen which enhances the well-known chemical transformation of methane to acetylene (Figure S4 in the supplementary material), explaining why we obtain graphene with methane at 700 °C (experiments D1 and OPT1). In our conditions, most of the methane introduced in the reactor is transformed to acetylene in a few milliseconds. We performed numerical calculations to simulate the plasma composition by considering a detailed kinetics for the decomposition of the methane in the experiments associated with this paper. Our model solves the coupled energy and mass problem in the specific microwave plasma conditions. Figure S5 in the supplementary material clearly shows this behavior.

In addition, thermal CVD of graphene is performed, in general, in hot-wall type reactor where gas temperature can reach at maximum of about 1000 °C. Since the chemical transformation of methane to acetylene requires a temperature higher than 1000 °C, the graphene deposition with hot-wall reactor is limited to carbon precursors with lower dissociation barrier, such as acetylene. In the present study, we used cold-wall type reactor where plasma temperature as high as 2000 °C can be achieved, suggesting that graphene deposition at low temperature is possible even if methane is used as precursor. In this case, dissociated species and acetylene diffuse to the surface where they participate to graphene growth.

D. STM characterization of the transferred graphene films

In order to characterize the structural properties of the graphene sample OPT3 after transfer, we performed STM experiments on graphene transferred on a Au(111) substrate. The measurements were performed under ultra-high vacuum conditions (10^{-10} mbar) and at room temperature. The Au(111)/mica substrate was cleaned by repeated cycles of Ar+ ion sputtering and annealing at 300 °C. The sample was then taken out from the UHV system to transfer the graphene sheet in ambient condition. Then, the sample was introduced again in the UHV system and degassed at 100 °C.

In the large-scale image reported in Figure 8(a), white linear structures are observed that likely correspond to graphene ripples with typical heights of 1 nm. The surface shown in this image appears to be 100% covered by graphene. The atomic resolution images in the inset of Figure 8(a) reveal the honeycomb lattice of the graphene sheet. In addition, Moiré patterns are observed on the sample (see Figure 8(b)), indicating that the sample is made of bilayer or multilayer graphene. In Figure 8(b), thin lines corresponding to rotational grain boundaries can be seen. In domains 1 and 2 of Figure 8(b), Moiré patterns can be observed with different periods, indicating that the graphene layer has two different orientations in these domains. The periods of the Moiré patterns are found to be 7.8 nm in domain 1 and 2.2 nm in domain 2. These periods correspond to a Moiré pattern between two graphene layers rotated by 1.8° and 6.3°, respectively.[48] This means that the corresponding grain boundary separates two domains of graphene that are rotated by 4.5°. Such a low angle grain boundary is expected to be buckled,[49] as evidenced by the series of bumps observed along the grain boundary in the STM image. The ripples and grain boundaries are the only defects of the graphene layer observed in the images of Figure 8, showing the high quality of the graphene sheet in these areas; in particular, we did not

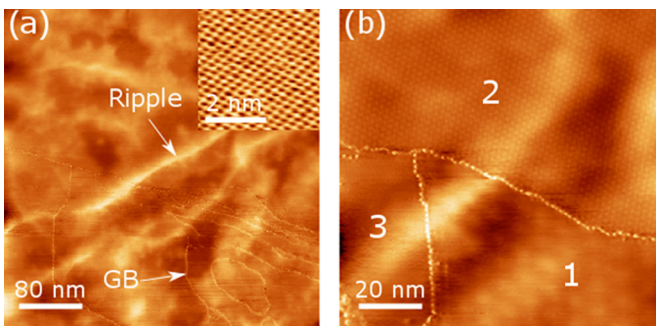

FIG. 8. Room temperature STM images of the graphene films (obtained in OPT3), after undergoing transfer on Au (111)/mica substrate. (a) Large scale image (obtained at 100 mV, 800 pA) where ripples and grain boundaries (GB) can be observed. The inset shows the atomic resolution of the graphene sheet. (b) Area with 3 graphene domains separated by rotational grain boundaries (obtained at 1 V, 800 pA). Different Moiré patterns are observed on domains 1 and 2.

observe point defects or more complex defects in the graphene domains.

IV. CONCLUSION

In this work, a microwave plasma-enhanced chemical vapor deposition (PECVD) system is used to synthesize graphene on cobalt substrates. The process is based on the cobalt-catalyzed decomposition of hydrogen-methane mixture followed by carbon saturation of the cobalt substrate at high temperature. While cooling the substrate, the solubility of carbon in the cobalt decreases, and a thin film of carbon is thought to precipitate from the surface. Substrate temperature, methane flow rate, deposition time, and microwave power were assumed to affect the graphene number of layers and defect density. To simultaneously optimize these two structural parameters in a reduced number of experiments, each control factor was varied within two levels, using Taguchi method. Conducting the sensitivity analysis and performing analysis of variance (ANOVA) have allowed obtaining definite information about the weightage of parameters, thereby ranking all the parameters individually on overall crystalline quality and thickness of the graphene. In the parameter range considered, substrate temperature was found to be most influential. Its percentage contribution is 42% on number of graphene layers and 64% on defect density. Nevertheless, based on signal-to-noise statistical analysis, the value of the criteria failed to meet the expectation, indicating that interactions occur between the parameters. To determine the graphene films' homogeneity over the substrate, Raman mapping was performed over an area of $100 \times 100\,\mu m^2$ and a large portion of the surface was covered with few-layer graphene with a good crystallinity. To quantitatively estimate the layer thicknesses, as-grown graphene films were transferred from Co substrates to the TEM grid by electrochemical bubbling using a polymer support. High resolution transmission electron microscopy (HRTEM) and the Fourier transform of HRTEM images allow to characterize (2–7) twisted-multilayer graphene and to view individual atoms. Scanning tunneling microscopy (STM) was used to direct visualization of the graphene lattice, identify rotational grain boundaries, and reveal the multilayer nature of the investigated sample areas through the presence of Moiré patterns. To clarify the role of each growth parameter, a systematic study using thermochemical modeling is currently in progress.

SUPPLEMENTARY MATERIAL

See supplementary material for the typical steps in PECVD graphene growth on high carbon solubility substrates and most influential parameters in each step, SEM image of the sample OPT3, HRTEM image of multilayer graphene with a Bernal structure, a schema for simplified chemical transformation of methane to acetylene, and thermochemical simulation of the methane dissociation in microwave plasma.

ACKNOWLEDGMENTS

IFR Paris Nord Plaine de France (PPF), ANR (Agence Nationale de la Recherche), and CGI (Commissariat à l'Investissement d'Avenir) are gratefully acknowledged for their financial support of this work through Labex SEAM (Science and Engineering for Advanced Materials and devices) ANR 11 LABX 086, ANR 11 IDEX 05 02, and ANR-14-CE08-0018.

[1]K. S. Novoselov, A. K. Geim, S. V. Morozov, D. Jiang, Y. Zhang, S. V. Dubonos, I. V. Grigorieva, and A. A. Firsov, Science **306**, 666 (2004).
[2]A. C. Neto, F. Guinea, N. Peres, K. Novoselov, and A. Geim, Rev. Mod. Phys. **81**, 109 (2009).
[3]C. Lee, X. Wei, J. W. Kysar, and J. Hone, Science **321**, 385 (2008).
[4]A. A. Balandin, S. Ghosh, W. Bao, I. Calizo, D. Teweldebrhan, F. Miao, and C. N. Lau, Nano Lett. **8**, 902 (2008).
[5]C. Berger, Z. Song, X. Li, X. Wu, N. Brown, C. Naud, D. Mayou, T. Li, J. Hass, A. N. Marchenkov, E. H. Conrad, P. N. First, and W. A. de Heer, Science **312**, 1191 (2006).
[6]K. V. Emtsev, A. Bostwick, K. Horn, J. Jobst, G. L. Kellogg, L. Ley, J. L. McChesney, T. Ohta, S. A. Reshanov, J. Rohrl, E. Rotenberg, A. K. Schmid, D. Waldmann, H. B. Weber, and T. Seyller, Nat. Mater. **8**, 203 (2009).
[7]M. Choucair, P. Thordarson, and J. A. Stride, Nat. Nanotechnol. **4**, 30 (2009).
[8]S. Stankovich, D. A. Dikin, R. D. Piner, K. A. Kohlhaas, A. Kleinhammes, Y. Jia, Y. Wu, S. T. Nguyen, and R. S. Ruoff, Carbon **45**, 1558 (2007).
[9]S. Park and R. S. Ruoff, Nat. Nanotechnol. **4**, 217 (2009).
[10]P. W. Sutter, J-I. Flege, and E. A. Sutter, Nat. Mater. **7**, 406 (2008).
[11]X. Li, W. Cai, J. An, S. Kim, J. Nah, D. Yang, R. Piner, A. Velamakanni, I. Jung, E. Tutuc, S. K. Banerjee, L. Colombo, and R. S. Ruoff, Science **324**, 1312 (2009).
[12]M. S. Dresselhaus, G. Dresselhaus, and P. Avouris, *Carbon Nanotubes: Synthesis, Structure, Properties, and Applications* (Springer, Berlin, 2001).
[13]G. Malandrino, *Chemical Vapour Deposition: Precursors, Processes and Applications*, edited by A. C. Jones and M. L. Hitchman (Angewandte Chemie International Edition, 2009), Vol. 48, p. 7478.
[14]T. Oznuluer, E. Pince, E. O. Polat, O. Balci, O. Salihoglu, and C. Kocabas, Appl. Phys. Lett. **98**, 183101 (2011).
[15]E. Kim, H. An, H. Jang, W.-J. Cho, N. Lee, W.-G. Lee, and J. Jung, Chem. Vap. Deposition **17**, 9 (2011).
[16]J. Coraux, T. N'Diaye, M. Engler, C. Busse, D. Wall, N. Buckanie, F. J. M. zu Heringdorf, R. van Gaste, B. Poelsema, and T. Michely, New J. Phys. **11**, 023006 (2009).
[17]K. S. Kim, Y. Zhao, H. Jang, S. Y. Lee, J. M. Kim, K. S. Kim, J-H. Ahn, P. Kim, J-Y. Choi, and B. H. Hong, Nature **457**, 706 (2009).
[18]A. Reina, X. Jia, J. Ho, D. Nezich, H. Son, V. Bulovic, M. Dresselhaus, and J. Kong, Nano Lett. **9**, 30 (2009).
[19]S-Y. won, C. V. Ciobanu, V. Petrova, V. B. Shenoy, J. Bareno, V. Gambin, I. Petroy, and S. Kodambaka, Nano Lett. **9**, 3985 (2009).
[20]T. Fujita, W. Kobayashi, and C. Oshima, Surf. Interface Anal. **37**, 120 (2005).
[21]C. M. Seah, S. P. Chai, and A. R. Mohamed, Carbon **70**, 1 (2014).
[22]C.-T. Au, C.-F. Ng, and M.-S. Liao, J. Catal. **185**, 12 (1999).
[23]L. Gao, W. Ren, H. Xu, L. Jin, Z. Wang, T. Ma, L.-P. Ma, Z. Zhang, Q. Fu, L.-M. Peng, X. X. Bao, and H.-M. Cheng, Nat. Commun. **3**, 699 (2012).
[24]D. G. Goodwin and J. E. Butler, *Handbook of Industrial Diamonds and Diamond Films* (Marcel Dekker, Inc., 1997).
[25]J. Wang, M. Zhu, R. A. Outlaw, X. Zhao, D. M. Manos, and B. C. Holloway, Carbon **42**, 2867 (2004).
[26]A. Malesevic, R. Vitchev, K. Schouteden, A. Volodin, L. Zhang, G. V. Tendeloo *et al.*, Nanotechnology **19**, 305604 (2008).
[27]G. D. Yuan, W. J. Zhang, Y. Yang, Y. B. Tang, Y. Q. Li, J. X. Wang *et al.*, Chem. Phys. Lett. **467**, 361 (2009).
[28]M. Kim, N. S. Safron, E. Han, M. S. Arnold, and P. Gopalan, Nano Lett. **10**, 1125 (2010).
[29]J. Kim, M. Ishihara, Y. Koga, K. Tsugawa, M. Haseqawa, and S. Iijima, Appl. Phys. Lett. **98**, 091502 (2011).
[30]Z. Bo, Y. Yang, J. Chen, K. Yu, J. Yan, and K. Cen, Nanoscale **5**, 5180 (2013).
[31]J. Sun, Y. Chen, M. Kr. Priydarshi, Z. Chen, A. Bachmatiuk, Z. Zou, Z. Chen, X. Song, Y. Gao, M. H. Rummeli, and Y. Zhang, Nano Lett. **15**, 5846 (2015).

[32]G. Taguchi, Microelectron. Reliab. **37**, 381 (1997).
[33]S. Singh, Int. J. Adv. Eng. Manu. Technol. **63**, 1191 (2012).
[34]M. Pancielejko, A. Czyzniewski, V. Zavaleyev, A. Pander, and K. Wojtalik, Arch. Mater. Sci. Eng. **54**, 60 (2012).
[35]N. Ali, V. F. Neto, S. Mei, G. Cabral, Y. Kousar, E. Titus, A. A. Ogwu, D. S. Misra, and J. Gracio, Thin Solid Films **469**, 154 (2004).
[36]S. Santangelo, C. Milone, E. Piperopoulos, M. Lanza, and S. Galvagno, Mater. Res. Bull. **47**, 595 (2012).
[37]S. Santangelo, G. Messina, A. Malara, N. Lisi, T. Dikonimos, A. Capasso, L. Ortolani, V. Morandi, and G. Faggio, Diamond Relat. Mater. **41**, 73 (2014).
[38]L. Chen, Z. Kong, S. Yue, J. Liu, J. Deng, Y. Xiao, R. G. Mendes, M. H. Rümmeli, L. Peng, and L. Fu, Chem. Mater. **27**, 8230 (2015).
[39]C. Ricolleau, J. Nelayah, T. Oikawa, Y. Kohno, N. Braidy, G. Wang, F. Hue, L. Florea, V. P. Bohnes, and D. Alloyeau, Microscopy **62**, 283 (2013).
[40]P. A. Stadelmann, Ultramicroscopy **21**, 131 (1987).
[41]A. C. Ferrari and D. M. Basko, Nat. Nanotechnol. **8**, 235 (2013).
[42]L. M. Malard, M. A. Pimenta, G. Dresselhaus, and M. S. Dresselhaus, Phys. Rep. **473**, 51 (2009).
[43]C. Casiraghi, A. Hartschuh, H. Qian, S. Piscanec, C. Georgi, A. Fasoli, K. S. Novoselov, D. M. Basko, and A. C. Ferrari, Nano Lett. **9**, 1433 (2009).
[44]A. C. Ferrari, J. C. Meyer, V. Scardaci, C. Casiraghi, M. Lazzeri, F. Mauri, S. Piscanec, D. Jiang, K. S. Novoselov, S. Roth, and A. K. Geim, Phys. Rev. Lett. **97**, 187401 (2006).
[45]J.-B. Wu, X. Zhang, M. Ijäs, W.-P. Han, X.-F. Qiao, X.-L. Li, D.-S. Jiang, A. C. Ferrari, and P.-H. Tan, Nat. Commun. **5**, 5309 (2014).
[46]J. C. Meyer, S. Kurasch, H. J. Park, V. Skakalova, D. Künzel, A. Groß, A. Chuvilin, G. Algara-Siller, S. Roth, T. Iwasaki, U. Starke, J. H. Smet, and U. Kaiser, Nat. Mater. **10**, 209 (2011).
[47]J. Kim, J. Seo, H. K. Jung, S. H. Kim, and H. W. Lee, J. Ceram. Process. Res. **13**, Spec. 1, s42 (2012).
[48]T. A. Green and J. Weigle, Helv. Phys. Acta **21**, 217 (1948).
[49]Y. Tison, J. Lagoute, V. Repain, C. Chacon, Y. Girard, F. Joucken, R. Sporken, F. Gargiulo, O. V. Yazyev, and S. Rousset, Nano Lett. **14**, 6382 (2014).